



Cite this: *J. Mater. Chem. C*, 2018, **6**, 4225

Ordered three-fold symmetric graphene oxide/buckled graphene/graphene heterostructures on MgO(111) by carbon molecular beam epitaxy[†]

Chad Ladewig,^{‡,a} Tao Cheng,^{ID,‡,b} Michael D. Randle,^c Jonathan Bird,^c Opeyemi Olanipekun,^a Peter A. Dowben,^d Jeffry Kelber^{*a} and William A. Goddard III ^{ID,*b}

Theory and experiment demonstrate the direct growth of a graphene oxide/buckled graphene/graphene heterostructure on an incommensurate MgO(111) substrate. X-ray photoelectron spectroscopy, electron energy loss, Auger electron spectroscopy, low energy electron diffraction, Raman spectroscopy and first-principles density functional theory (DFT) calculations all demonstrate that carbon molecular beam epitaxy on either a hydroxylated MgO(111) single crystal or a heavily twinned thin film surface at 850 K yields an initial C layer of highly ordered graphene oxide with C_{3v} symmetry. A 5×5 unit cell of carbon, with one missing atom, forms on a 4×4 unit cell of MgO, with the three C atoms surrounding the C vacancy surface forming covalent C–O bonds to substrate oxide sites. This leads to a bowed graphene-oxide with slightly modified D and G Raman lines and a calculated band gap of 0.36 eV. Continued C growth results in the second layer of graphene that is stacked AB with respect to the first layer and buckled conformably with the first layer while maintaining C_{3v} symmetry, lattice spacing and azimuthal orientation with the first layer. Carbon growth beyond the second layer yields graphene in azimuthal registry with the first two C layers, but with graphene-characteristic lattice spacing and $\pi \rightarrow \pi^*$ loss feature. This 3rd layer is also p-type, as indicated by the 5.6 eV energy loss feature. The significant sp^3 character and C_{3v} symmetry of such heterostructures suggest that spin-orbit coupling is enabled, with implications for spintronics and other device applications.

Received 11th January 2018,
Accepted 14th March 2018

DOI: 10.1039/c8tc00178b

rsc.li/materials-c

Introduction

We present detailed theoretical and experimental results demonstrating how carbon molecular beam epitaxy (MBE) can result in the formation of graphene on an incommensurate polar oxide substrate, with significant implications for practical device applications. Direct graphene growth by scalable methods on dielectric substrates is a critical opportunity for the industrial-scale development of graphene-based devices. Attention has

naturally focused on lattice-commensurate substrates, particularly BN.^{1–3} However, growth on incommensurate polar oxides has also received attention,^{4–9} including substrates such as MgO,^{4,7–9} Co₃O₄(111),⁵ and Al₂O₃.⁶ Such incommensurate oxides are attractive because (a) this route to graphene growth would potentially make available a broader variety of substrates for various applications, and (b) substrate-graphene interactions might lead to novel graphene properties, such as a substrate-induced band gap,⁹ or induced spin polarization of graphene.^{10,11} The practical applications of such properties, however, require a detailed understanding of the graphene–polar oxide interfacial region, and of how the graphene is accommodated to a lattice-mismatched and chemically reactive substrate.

The experimental and theoretical results reported here provide, for the first time, such understanding and explain previously-observed graphene/MgO properties, such as the band gap.^{4,9,12} Moreover, the substantial sp^3 character and three-fold symmetry of the graphene oxide/graphene heterostructure strongly suggest the ‘turning on’ of spin-orbit coupling,¹³ with the potential for a substantial room-temperature spin Hall effect.¹⁴ The reproduction of similar results on both a highly ordered MgO(111) single crystal

^a Department of Chemistry, University of North Texas, 1155 Union Circle #305070, Denton, TX, USA. E-mail: Jeffry.Kelber@unt.edu

^b Materials and Process Simulation Center, California Institute of Technology, Pasadena, California 91125, USA. E-mail: wag@wag.caltech.edu

^c Department of Electrical Engineering, University at Buffalo, The State University of New York, Buffalo, NY 14260-1900, USA

^d Department of Physics and Astronomy, University of Nebraska-Lincoln, Lincoln, NE 68588-0299, USA

[†] Electronic supplementary information (ESI) available: AES spectra (Fig. S1), simple representation of two stacked lattices (Fig. S2) and the first layer of graphene on MgO before and after DFT optimization (Fig. S3). See DOI: 10.1039/c8tc00178b

[‡] Chad Ladewig and Tao Cheng contributed equally.

and heavily twinned thin film indicate that this interfacial arrangement can tolerate a substantial degree of substrate disorder, and suggest that such oxide/graphene heterostructures may be grown on other polar oxides with desirable properties. More broadly, these findings indicate that the ability to support graphene-to-oxide charge transfer is a predictive criterion for determining whether similar growth can be observed on other polar oxide substrates.

Experimental

MgO thin films were produced by DC-magnetron sputter deposition in a separate sputter deposition system on Ru(0001)/Al₂O₃(0001) substrates. The system and the preparation and characterization of Ru films have been described previously.¹⁵ MgO(111) films were prepared by deposition from an Mg target onto a Ru(0001)/Al₂O₃ substrate in an Ar plasma (8 mTorr Ar, 15 W) at 850 K in the same system as the Ru film deposition. This was followed by annealing in 10⁻⁶ Torr O₂ at 850 K. The MgO was then transferred to the main MBE/surface characterization chamber, described previously,¹⁵ and cleaned prior to C MBE by annealing in O₂ (10⁻⁶ Torr, 1000 K). Sample transfer from the MBE chamber to the surface-analysis chamber was accomplished without exposure to ambient. Subsequent Auger electron spectroscopy (AES) measurements showed no evidence of substrate Ru signal, indicating that the MgO(111) film thickness was greater than ~150 Å. Samples were then exposed to C MBE or subsequent annealing steps. AES, XPS, LEED and EELS data and analysis were carried out as previously described.¹⁵ Raman spectra were acquired *ex situ* using a 514 nm excitation source on a commercial instrument. Similar preparation and analysis methods were used for commercially available MgO(111) single crystals (1 cm × 1 cm × 1 mm).

C thickness calculations were carried out for both the MgO(111) single crystal and thin film by measuring the decrease in the O(KVV)/C(KVV) AES intensity ratio. Importantly, AES-derived average C carbon coverages are reported herein as monolayers, assuming a graphene monolayer (ML) equivalent of 3.3 Å ML⁻¹.¹⁶ Indeed, for graphene oxide with vacancies and non-planar character, and for buckled graphene layers (see below) this monolayer equivalence may be a considerable approximation. Therefore, the C coverages reported herein as monolayers must be regarded as approximate.

XPS and AES spectra were acquired on the clean MgO(111) single crystal or MgO thin film, respectively. The XPS spectra indicate significant hydroxylation of the single-crystal surface (*vide infra*), while AES spectra indicate an O/Mg atomic ratio of 1.2 : 1, also consistent with surface hydroxylation (see ESI,† Fig. S1) Such hydroxylation serves to stabilize the polar MgO(111) surface under ultrahigh vacuum conditions.¹⁷

C 1s and O 1s XPS spectra were deconvoluted into separate components corresponding to different chemical environments, in order to better interpret the results. Gaussian–Lorentzian lineshapes were used, with full-width-half-maxima values of 2.0 eV, based on the empirically determined energy resolution

of the analyzer under these conditions. For C 1s spectra, components with binding energies of 284.5, 285.5 and 287 eV were used for the sp² C, sp³ C, and the O-bonded C, respectively, based on previously reported results for diamond-like carbon.¹⁸ For the O 1s spectra, the binding energy of the major O component, corresponding to lattice O, was fixed to 531 eV based on published results in order to correct for peak shifts as a result of sample charging.¹⁹ The binding energy of the second component was allowed to vary to obtain the best fit to the experimental spectrum.

The quantum-mechanical calculations were carried out with the VASP software,^{20–22} using the PBE flavor²³ of density-functional theory (DFT). The projector augmented wave (PAW) method²⁴ was used to account for core–valence interactions. The kinetic energy cutoff for plane wave expansions was set to 500 eV, and reciprocal space was sampled by the Γ -centered Monkhorst–Pack scheme with a grid of 3 × 3 × 1. The surface slab consists of 4 × 4 × 2 MgO. The vacuum layer is at least 20 Å above the surface. The convergence criteria are 1 × 10⁻⁷ eV energy differences for solving the electronic wavefunction. The Methfessel–Paxton smearing of second order with a width of 0.1 eV was applied. All geometries (atomic coordinates) were converged to within 1 × 10⁻² eV Å⁻¹ for maximal components of forces. A post-stage vdW DFT-D3 method with Becke–Jonson damping was applied.²⁵

Results & discussion

Our DFT calculations for the O-terminated MgO(111) surface lead to the surprising indication that C MBE on this surface yields an initial graphene oxide layer (which we refer to as GraphOx to distinguish from other possible graphene oxide structures) with long-range order and *C_{3v}* symmetry (in Schoenflies notation). This is supported by experiment, as discussed below. Simply matching the unit of graphene to that of MgO(111) would lead to a lattice mismatch of 17.53%, but the 5 × 5 cell of graphene is only off from the area of the 4 × 4 of MgO(111) by 3.07%. We find a 5 × 5 layer unit cell of carbon with one missing C, with the three C surrounding the C vacancy forming covalent C–O bonds to substrate oxide sites (Fig. 1). That is, 12.5% of the C atoms in the first C layer form covalent bonds to the O sites on the MgO surface, resulting in substantial charge transfer from the C layer to the oxide. This involves a compression in the top layer that is accommodated by the vacancy, which leads to a bowed graphene-oxide (GraphOx) layer, with slightly modified D and G Raman lines and a calculated band gap of 0.36 eV.

The calculated interaction energies between the first C layer and unreconstructed, O-terminated MgO(111) are used to estimate the stability of the first C layer using the following definitions:

$$\Delta E_{\text{MgO-Graphene}} = \frac{E_{\text{MgO-Graphene}} - (n_{\text{Mg}} E_{\text{MgO}(111)} + n_{\text{C}} E_{\text{graphene}})}{n_{\text{C}}} \quad (1)$$

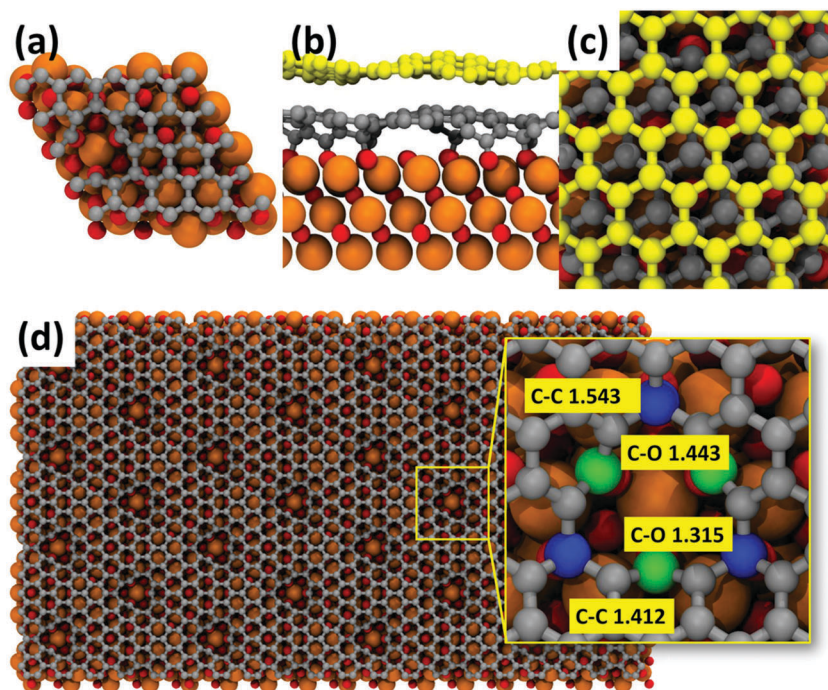


Fig. 1 DFT results for first and second layer C films on MgO(111) surface. (a) First layer contains 49 C atoms based on a 5×5 pattern from graphene, but with one missing C, lattice matched to a 4×4 cell of MgO, a distortion of 3.07% in the carbon layer. This leads to long-range C_{3v} symmetry (b) side view of first C layer (grey spheres) and second C layer (yellow spheres; O = red spheres, Mg = orange spheres); (c) calculated most-stable AB stacking configuration of the first (grey) and second (yellow) carbon layers; (d) extended array showing long range C_{3v} symmetry. The inset shows the details of bonding around each C_{3v} vacancy: three C (grey) each form a 1.315 Å covalent bonded to a substrate O (blue) while three other C carbon (green) form a 1.443 Å donor–acceptor bond with a substrate O (in red) leading to six C–C bonds around the vacancy of 1.543 Å while the other six C=C bonds are the normal 1.412 Å.

Here, $\Delta E_{\text{MgO-Graphene}}$ is the total energy of the graphene (or GraphOx) layer on MgO; $E_{\text{MgO}(111)}$ is the energy of MgO(111) surface per one MgO formula unit; E_{graphene} is the energy of single-layer graphene (GraphOx) per one C atom; n_{Mg} is 48 and n_{C} is 49. The calculated $\Delta E_{\text{MgO-Graphene}}$ is -0.28 eV per C atom or 13.7 eV per unit cell of GraphOx. This can be compared to the binding energy between two layers in graphite of 0.05 eV per C atom or 2.6 eV per 50 C atoms. This indicates that the chemisorbed GraphOx layer is stable on the MgO(111) surface.

The DFT calculations for the second layer of graphene find that it is stacked AB with respect to and buckled conformably with the first layer while maintaining C_{3v} symmetry and the azimuthal orientation with the first layer, as summarized graphically in Fig. 1b and c. For this second layer, we find the stability of 0.04 eV per 2nd C layer, which can be compared to 0.05 eV per C between two layers in graphite. The band gap for this layer drops to 0.084 eV, and the D–G lines are closer to those of graphene. A detailed top view of the first C layer is shown in Fig. 1d.

Local defects of 3-fold symmetry (Fig. 1a and d) form due to covalent bond formation between C atoms and the substrate. As shown in Fig. 1d, these defects are arrayed to yield long-range C_{3v} symmetry, and the lattice spacing of the GraphOx layer is commensurate with the lattice spacing of the MgO(111) substrate. This involves the GraphOx layer accommodating a lattice mismatch of $\sim 20\%$ with the O-terminated MgO

substrate, achieved with significant non-planarity (Fig. 1b). The second C layer also exhibits significant non-planarity (Fig. 1c) but without a missing carbon atom. The DFT results also show that such interaction results in significant buckling of the first C layer. The charge transfers and reduction of sp^2 hybridization due to non-planarity of this layer should significantly deplete the π electron system,

These surprising and unexpected results from DFT led us to carry out a series of experiments, including *in situ* x-ray photo-electron spectroscopy (XPS), characteristic electron energy loss spectroscopy (EELS), low energy electron diffraction (LEED), Auger electron spectroscopy (AES) and ex-situ Raman measurements on both a hydroxylated MgO(111) single crystal and on a heavily twinned MgO(111)/Ru(0001)/Al₂O₃(0001) thin film. All these experimental results are consistent with the DFT calculations, confirming the formation of a GraphOx first layer and a conformal AB stacked 2nd layer.

The C 1s XPS spectra and corresponding LEED and EELS data are shown in Fig. 2 for C MBE at 850 K on the hydroxylated MgO(111) single crystal surface. No significant change in the Mg 2p or O 1s spectra (not shown) were observed during the deposition process. The C 1s XPS spectra (Fig. 2a–c) are broad, showing that, at coverages of 2 or fewer C MLs, many of the C atoms are in oxidized states. Deconvolution of the spectra into three distinct components reveals that a portion of each C 1s spectrum is attributable to a component at 287 eV, indicative of

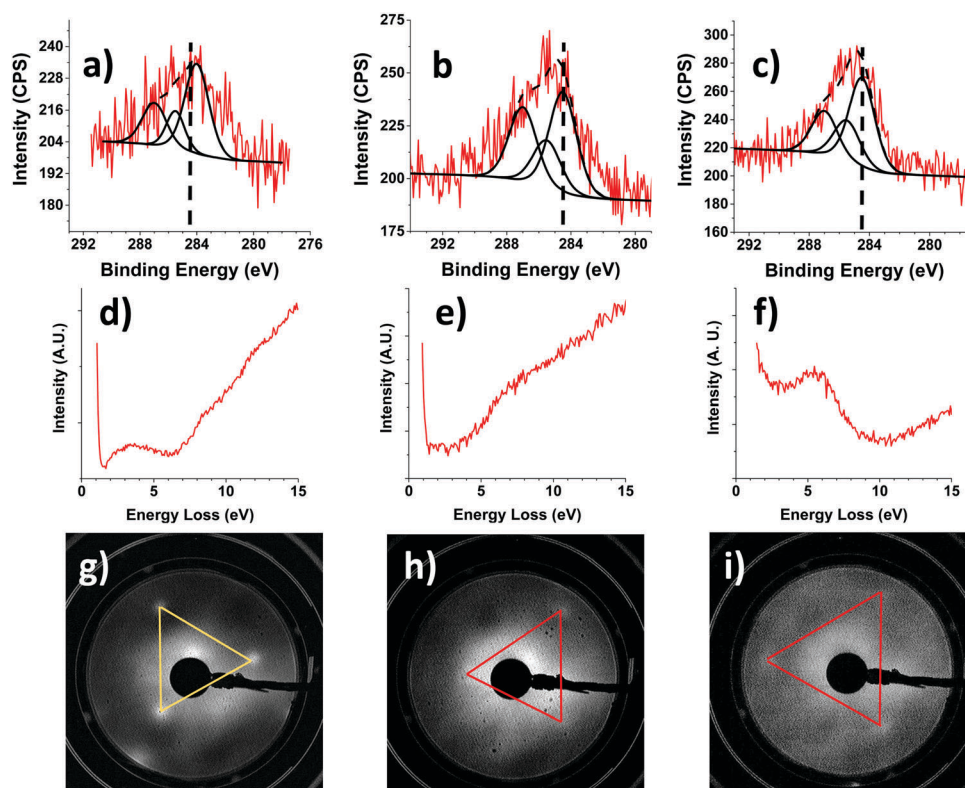


Fig. 2 (a–c) C 1s XPS spectra for average C coverages of 1, 2 and 3 MLs, respectively; (d–f) corresponding EELS spectra (g–i) corresponding LEED data; EELS excitation energy 100 eV. LEED beam energy (g and h) 100 eV and (i) 250 eV. Triangles (g–i) are guides to the eye.

C–O bond formation.¹⁸ The two remaining components positioned at 284.5 and 285.5 eV, indicate the presence of both sp^2 carbon as expected in graphene and sp^3 carbon due to the buckling of the first two carbon layers.¹⁸ Quantification of the component intensities shows that the area under the C–O feature is ~25% of the total C 1s intensity after ~1 ML C. This is roughly twice the prediction of the DFT calculations. This suggests that this feature includes adjacent C atoms (see Fig. 1) that are also strongly polarized by the strong C to oxide charge transfer. At a coverage of ~2 ML C, a broad C 1s peak maximum is observed from ~285.5 eV to 285 eV, which is significantly higher than the 284.5 eV generally considered characteristic of undoped graphene. These data are consistent with electron charge transfer from both graphene layers to the magnesium oxide substrate, and a substantial sp^3 character in the second C layer^{5,26} At a C coverage of ~3 MLs, however, a C 1s peak maximum near 284.5 eV is apparent. Sample charging during LEED acquisition increased considerably with C coverage, and at coverages of ~3 MLs, a beam energy of 250 eV was necessary for image acquisition. Therefore, the LEED image at 3 ML C coverage (Fig. 2i) cannot be compared directly to LEED images (Fig. 2g and h) acquired at 1 or 2 ML coverages at 100 eV beam energy. However, the LEED image taken at a higher beam energy does contain signal from both the top two layers giving insight for comparison of the 2nd and 3rd carbon layers. Due to a similar pattern observed between Fig. 2h and i, the LEED image at 3 ML C coverage indicates the presence of long-range

order and 3-fold symmetry in this layer as in the other two C layers. For all C coverages, the LEED spots are fainter than for the clean surface, as expected due to the reduced scattering power of C relative to Mg or O.²⁷

The EELS spectra (Fig. 2d and e) exhibit a broad, low-intensity loss feature below ~5 eV for 1 ML of C and the absence of a loss feature below ~5 eV for 2 MLs. The absence of a loss feature at ~5 eV for the 2 ML film is attributed to the inclusion of a rising background in the spectra preventing observation of the feature. The broad feature in Fig. 2d is not related to MgO²⁸ and does not correspond to the relatively intense $\pi \rightarrow \pi^*$ feature characteristic of graphene.²⁹ At a C coverage of 3 MLs, however, such a graphene-characteristic $\pi \rightarrow \pi^*$ feature is observed, albeit with a peak maximum near 5.6 eV. This peak loss energy is significantly higher than the value of ~5.0 eV observed for few-layer undoped graphene,²⁹ indicating that there is still some charge transfer from this third C layer to the substrate. In summary, the data in Fig. 2 indicate that the first two C layers produced by MBE at 850 K on hydroxylated MgO(111) are heavily p-doped, and exhibit long-range order with C_{3v} symmetry and the lattice spacing of the MgO substrate. The third C layer exhibits C 1s XPS and EELS spectra more characteristic of graphene, but with evidence of p-type doping.

A closer look at the LEED data, acquired at different energies at 1 ML and 1.5 ML C coverages (Fig. 3), provides further insight concerning the transition from the first to the second C layer.

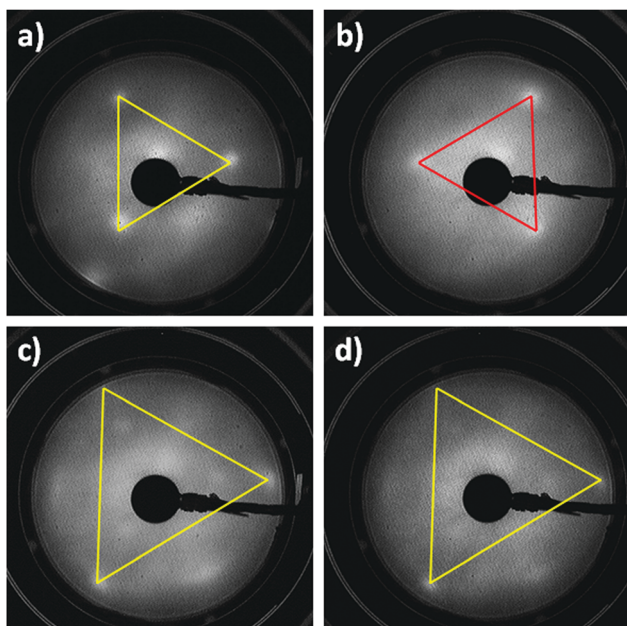


Fig. 3 (a and b) LEED data (beam energy 100 eV) acquired at 1 and 1.5 ML C coverages, respectively; (c and d) corresponding data at 150 eV. Triangles are guides to the eye.

LEED images acquired at 100 eV beam energy for \sim 1.5 MLs of C coverage (Fig. 3b) show a 60° rotation of the 3-fold LEED pattern with respect to those acquired at lower C coverages (Fig. 3a). No such rotation is observed for the corresponding LEED images acquired at 150 eV (Fig. 3c and d). The LEED images taken at higher C coverages showed no further change from those observed in Fig. 3b and d. This LEED behavior

indicates a buckling corresponding to a displacement along the normal to the graphene layer, of either the A or B site carbon atoms, during formation of the second C layer.³⁰ The fact that the C_{3v} symmetry of the second layer appears to be rotated with respect to the C_{3v} symmetry of the first layer does not indicate C_{6v} symmetry, but rather a preservation of C_{3v} symmetry as a result a relative vertical displacement of either the "A" or "B" sites in the graphitic (graphene-like) second layer lattice plane.³⁰ Thus, the LEED data acquired at 100 eV indicate that the second graphene layer is non-planar and "buckled". LEED data acquired at higher energy, however, indicate that the second layer lattice is nonetheless still ordered with C_{3v} symmetry, and in azimuthal alignment with the first layer and with the MgO(111) substrate.

The O 1s XPS spectra are shown in Fig. 4 as a function of C overlayer thickness. These spectra have been deconvoluted using a feature at 531.0 eV, corresponding to lattice oxygen.¹⁹ The binding energy of the second component was allowed to vary in order to obtain the best fit, giving the binding energy of \sim 533 eV, corresponding to OH species.¹⁷ The degree of surface hydroxylation was estimated by assuming that only the first O layer of the MgO(111) crystal contains OH groups and that the intensity of the lattice O feature includes attenuated intensity from subsurface O layers.¹⁵ The relative intensity of the OH feature in Fig. 4a thus indicates that, prior to C deposition, greater than 90% of the surface O atoms are in fact hydroxyl species, consistent with previous studies showing that hydroxylation of the (111) surfaces of MgO and similar polar oxides stabilizes the (111) structure against reconstruction.¹⁷ C deposition, however (Fig. 4b-d) results in a monotonic decrease in relative OH intensity (see inset, Fig. 4b). Deposition of the first C layer results in a decrease in relative OH intensity of \sim 10%, in general agreement

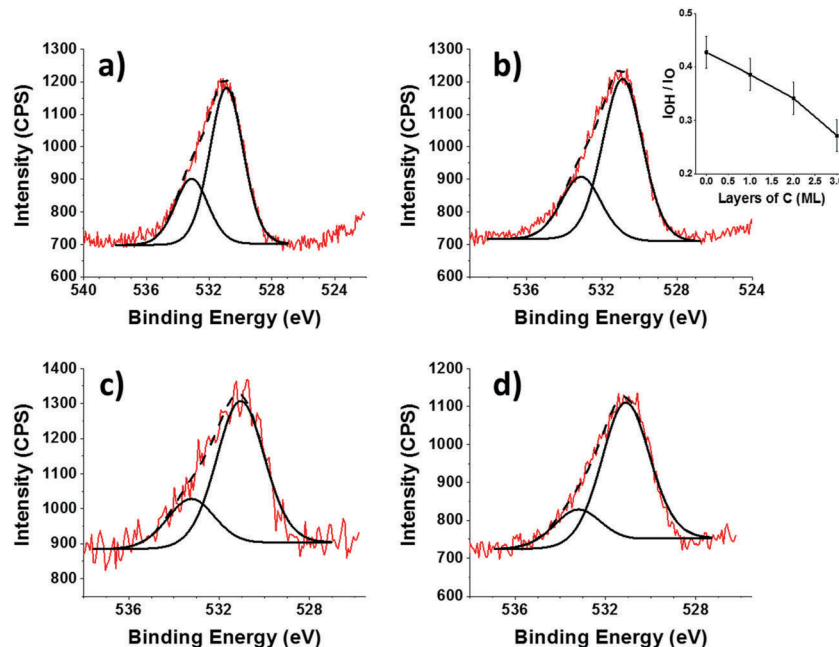


Fig. 4 (a-d) O 1s XPS spectra of 0 ML, 1 ML, 2 ML and 3 ML carbon coverage on a MgO(111) single crystal respectively. Inset in (b) corresponds to the ratio of intensities for the OH (higher binding energy) and O (lower binding energy) components as a function of carbon coverage in ML ($3.3 \text{ \AA} = 1 \text{ ML}$).

with the DFT calculations regarding the extent of the C-O bond formation. The data also show, however, that subsequent C deposition beyond the first C ML continues to decrease the relative degree of surface hydroxylation, suggesting that either C/surface reactions continue after 1 C ML, or possibly that OH destruction *via* desorption of H₂ occurs at reaction temperatures, without re-hydroxylation by reaction with background gases in the chamber.

The EELS spectra and LEED images acquired for a heavily twinned MgO(111)-oriented thin film are compared in Fig. 5 for average C coverages of 0, 1.0, and 2.7 MLs. The EELS data (Fig. 5a–c) show a similar trend as for the MgO(111) single crystal, with the formation of a well-developed $\pi \rightarrow \pi^*$ feature near 5.8 eV at average C coverages approaching 3 MLs. Sample charging during LEED acquisition was much less severe on this substrate than on the single crystal, allowing image acquisition at beam energies as low as 60 eV. LEED data and corresponding line scans (Fig. 5d–f) also show a similar trend, with images and scans from a sample with \sim 2 MLs average C thickness, very similar to that of the clean substrate.

One major difference observed between the LEED images in Fig. 5d and e is the twinning at each of the 12 major spots in Fig. 5d, corresponding to the clean MgO surface, and the disappearance of such twinning upon deposition of \sim 1 ML C, as in Fig. 5e. This demonstrates that the twinning observed in Fig. 5d is related to the vicinal MgO surface, and not the C

overlayer. The twinning of the vicinal MgO film could be produced by portions of the topmost two atomic layers being rotated 30° with respect to one another as a result of the MgO film deposition. A model of an arbitrary (111) surface of a rocksalt structure AB crystal was created, followed by rotation of the topmost layer by 30° with respect to the second layer (see Fig. S2, ESI†), resulting in a direct space structure that would yield a reciprocal space image such as observed in Fig. 5d. The LEED data from the third layer, however, exhibit the larger indirect lattice spacing characteristic of graphene. Additionally, several faintly bifurcated spots can be observed in the LEED image corresponding to 2.7 MLs average coverage (Fig. 5f – inset) indicating the formation of the graphene-like overlayer on top of the second carbon layer which exhibits a smaller inverse lattice constant. Therefore, the data in Fig. 5 demonstrate that C MBE growth on the twinned surface of an MgO(111) thin film displays the same trends as on a highly ordered, hydroxylated MgO(111) single crystal. The first and second C layers are conformal to the MgO substrate, while the third layer exhibits the EELS and LEED spectra expected of graphene.

These LEED data (Fig. 2g and h) for average C coverages up to 2 ML are in agreement with the DFT, and the substantial charge transfer from the C layer to the oxide calculated agrees with C 1s XPS data (Fig. 2a–c). The charge transfer and reduction of sp² hybridization due to non-planarity of the 2nd layer significantly depletes the π electron system, which is

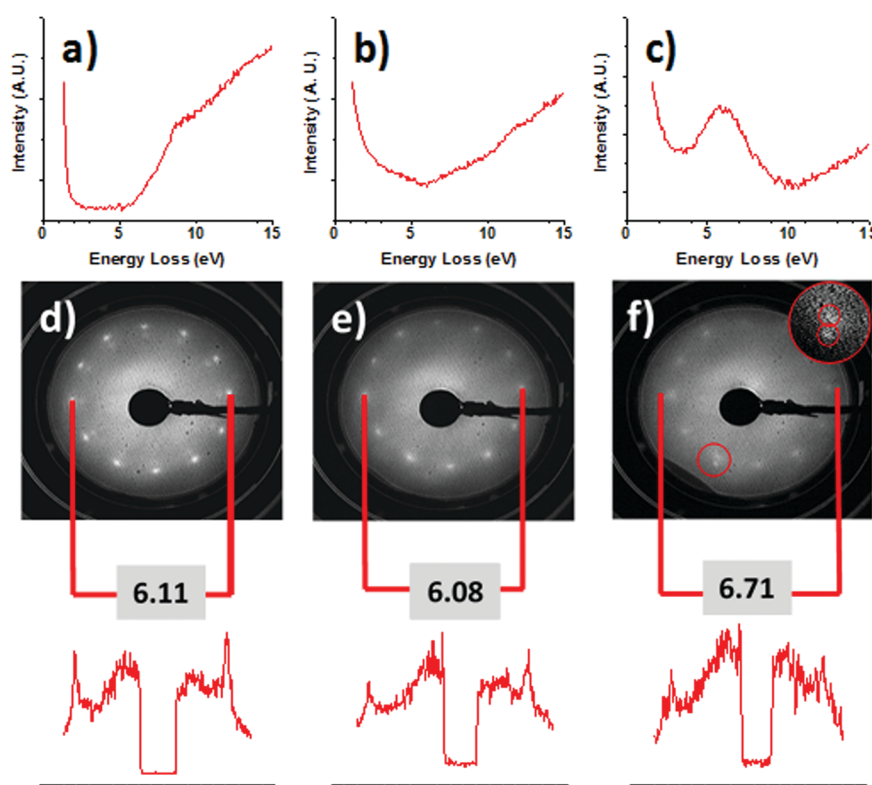


Fig. 5 (a–c) EELS spectra for C films deposited on a MgO thin film with average C coverages of 0 ML, 1.3 ML and 2.7 MLs, respectively. (d–f) Corresponding LEED images with cross sections (inset in f) demonstrating the bifurcated spots indicating the third C layer has a smaller direct lattice spacing than the first two C layers. Numbers in (d–f) correspond to distances, in pixels between corresponding LEED spots and are inversely proportional to the direct space lattice constant. EELS spectra acquired at 100 eV; LEED images acquired at 60 eV.

entirely consistent with the EELS features for the first two C layers on both the MgO(111) single crystal (Fig. 2d and e) and the thin film (Fig. 4a and b).

The LEED data for both the single crystal and thin film also exhibit the predicted, second C non-planar layer conformal to the non-planarity of the first layer, as shown in Fig. 1b (Fig. 2h and 5e, respectively). The EELS data, (Fig. 2e and 5b) are also consistent with the DFT results, indicating that at 2 MLs average C thickness, a substantial $\pi \rightarrow \pi^*$ loss feature is not observed. The C 1s XPS data displayed in Fig. 1a and b are also consistent with the DFT-predicted non-planarity and general conformity of the second C layer to the first (Fig. 1b). This strongly suggests substantial electronic coupling and charge transfer between the layers and the substrate; experiments are in agreement with the DFT in describing the first and second C layer as highly p-doped, with C_{3v} symmetry and the lattice spacing of the first layer.

The experimental and calculated Raman spectra are compared in Fig. 6. The *ex situ* experimental spectrum was acquired for 2.7 ML C coverage on the MgO(111) film (see Methods). The experimental spectrum is similar to other reported Raman spectra for graphene oxide.^{31,32} Specifically, the relatively large intensity and breadth of the ‘‘D’’ feature—typically associated with defects in graphene layers—is consistent with the substantial sp^3 character of the first two graphene layers, as indicated by both experiment and theory. A calculated spectrum for the single phonon region of the first layer (Fig. 6, inset) is shown in comparison. The lack of a second buckled layer with the sp^3 character in the simulation yields a lower relative D peak intensity. The experimental Raman spectrum, while confirming the presence of graphene oxide and consistent with an additional layer of buckled graphene, does not rule out the existence of a third, graphene or graphene-like layer, due to the greater intensities of the graphene oxide-related features.

Summary and conclusion

In summary, experimental and theoretical results shown here demonstrate that C MBE on OH-stabilized MgO(111) yields an initial highly ordered graphene oxide layer with C_{3v} symmetry

and the lattice spacing of the MgO substrate. The second C layer does not contain C–O bonds but is still significantly p-doped, buckled, and maintains the same lattice spacing as the GraphOx and MgO surface. Only upon formation of a third C layer is graphene-like character found, with LEED indicating the expected smaller direct lattice spacing, and EELS displaying the expected $\pi \rightarrow \pi^*$ feature, albeit at an energy that still suggests some p-type doping of this layer.

Multiple device applications suggest themselves for the graphene oxide/buckled graphene/graphene system. The band gap of graphene oxide^{4,9,12,33} makes this material of general interest for a variety of sensor applications.^{34–36} As noted above, the C_{3v} symmetry and significant sp^3 character of at least the first two C layers on MgO(111) indicate that spin-orbit coupling should be enabled in these layers.¹³ Since transferred planar graphene with sparse sp^3 defects exhibits a significant room temperature spin Hall effect,¹⁴ our results suggest strongly that the C heterostructure produced by C MBE on MgO(111) should also exhibit such an effect. Thus, C MBE on MgO(111) provides a potential route towards the practical fabrication of a room temperature spintronics device without the use of either magnetic materials or externally applied magnetic fields.

The similar behavior observed on both a highly ordered MgO(111) single crystal and a twinned thin-film substrate indicate that the formation of this graphene oxide/buckled graphene/graphene interface is not overly dependent on precise substrate ordering. Instead, the graphene oxide acts as a buffer layer, assuming the lattice constant of the substrate. Indeed, similar experimental Raman spectra as in Fig. 6 have been obtained for few-layer ‘‘nano-graphene’’ produced by CH₄/H₂ chemical vapor deposition on MgO(001).⁸ Additionally, similar behavior, including the formation of an initial graphene oxide layer, has been reported for C MBE on Co₃O₄(111), but not on Cr₂O₃(0001), even though both are polar oxides with similar in-plane lattice spacings.⁵ Our DFT calculations indicate substantial charge transfer from a graphene layer to an adjacent Co₃O₄(111) layer.^{5,37} In contrast, similar calculations for a graphene/Cr₂O₃(0001) interface indicate that charge transfer should flow in the opposite direction—from the chromia to the graphene.³⁸ Since C–oxygen bond formation must involve charge transfer from the graphene layer to the oxide, it would

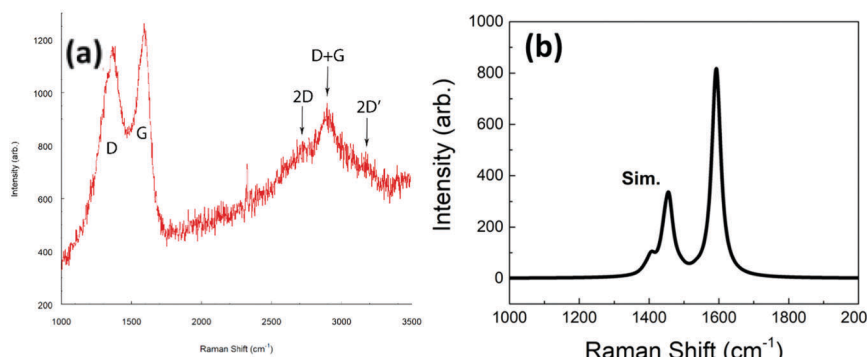


Fig. 6 (a) Experimental Raman spectrum of 2.7 ML C film on a MgO thin film; (b) the simulated Raman spectrum of 1 ML C film on a MgO thin film.

appear that such interfacial charge transfer calculations have predictive value for determining whether the C heterostructure formation presented here occurs for other polar oxide surfaces. Finally, the above theoretical results were obtained for an O-terminated MgO(111) surface, but agree in detail with experimental data for hydroxyl-stabilized¹⁶ MgO(111) surfaces. Such detailed agreement strongly suggests that surface OH groups are not an inhibitor of C–O covalent bond formation across the graphene/MgO interface.

Conflicts of interest

There are no conflicts to declare.

Acknowledgements

Work at UNT was supported by was supported by the NSF under grant no. ECCS-1508991, and in part by C-SPIN, a funded center of STARnet, a Semiconductor Research Corporation (SRC) program sponsored by MARCO and DARPA under task IDs 2381.001 and 2381.006. Work at Buffalo was supported by the NSF under the grant No. ECCS-1509221. Work at UNL was supported by the NSF under grant No. ECCS-1508541. Work at Caltech was supported as part of the Computational Materials Sciences Program funded by the U.S. Department of Energy, Office of Science, Basic Energy Sciences, under Award Number DE-SC00014607. This work used the Extreme Science and Engineering Discovery Environment (XSEDE), which is supported by National Science Foundation grant number ACI-1548562.

References

- W. Yang, G. Chen, Z. Shi, C. Liu, L. Zhang, G. Xie, M. Cheng, D. Wang, R. Yang, D. Shi, K. Watanabe, T. Taniguchi, Y. Yao, Y. Zhang and G. Zhang, *Nat. Mater.*, 2013, **12**, 792–798.
- M. S. Driver, J. D. Beatty, O. Olanipekun, K. Reid, A. Rath, P. M. Voyles and J. A. Kelber, *Langmuir*, 2016, **32**, 2601–2607.
- J. Dabrowski, G. Lippert, T. Schroeder and G. Lupina, *Appl. Phys. Lett.*, 2014, **105**, 191610.
- L. Kong, C. Bjelkevig, S. Gaddam, M. Zhou, Y. H. Lee, G. H. Han, H. K. Jeong, N. Wu, Z. Zhang, J. Xiao, P. A. Dowben and J. A. Kelber, *J. Phys. Chem. C*, 2010, **114**, 21618–21624.
- J. Beatty, T. Cheng, Y. Cao, M. S. Driver, W. A. Goddard III and J. A. Kelber, *J. Phys. Chem. Lett.*, 2017, **8**, 188–192.
- M. A. Fanton, J. A. Robinson, C. Puls, L. Yiu, M. J. Hollander, B. E. Weiland, M. A. Labelia, K. Trumbell, R. Kasarda, C. Howsare, J. Stitt and D. W. Snyder, *ACS Nano*, 2011, **5**, 8062–8069.
- J. Sun, T. Gao, X. Song, Y. Zhao, Y. Lin, H. Wang, D. Ma, Y. Chen, W. Xiang, J. Wang, Y. Zhang and Z. Liu, *J. Am. Chem. Soc.*, 2014, **136**, 6574–6577.
- M. H. Rummeli, A. Bachmatiuk, A. Scott, F. Bornert, J. H. Warner, V. Hoffman, J. Lin, G. Cuniberti and B. Buchner, *ACS Nano*, 2010, **4**, 4206–4210.
- R. Skomski, P. A. Dowben, M. S. Driver and J. A. Kelber, *Mater. Horiz.*, 2014, **1**, 563–571.
- Y. Wang, L. Kong, F. L. Pasquale, Y. Cao, B. Dong, I. Tanabe, C. Binek, P. A. Dowben and J. A. Kelber, *J. Phys.: Condens. Matter*, 2013, **25**, 472203.
- H. Haugen, D. Huertas-Hernando and A. Bratas, *Phys. Rev. B: Condens. Matter Mater. Phys.*, 2008, **77**, 115406.
- S. Gaddam, C. Bjelkevig, S. Ge, K. Fukutani, P. A. Dowben and J. A. Kelber, *J. Phys.: Condens. Matter*, 2011, **23**, 072204.
- D. Kochan, S. Irmer and J. Fabian, *Phys. Rev. B*, 2017, **95**, 165415.
- J. Balakrishnan, G. Koon Kok Wai, M. Jaiswal, A. H. Castro Neto and B. Ozilimaz, *Nat. Phys.*, 2013, **9**, 284–287.
- O. Olanipekun, C. Ladewig, T. Estrada, J. A. Kelber, M. D. Randle, J. Nathawat, C. Kwan, J. P. Bird, P. Chakraborti, P. A. Dowben, T. Cheng and W. A. Goddard III, *Semicond. Sci. Technol.*, 2017, **32**, 095011. For a description of basic data analysis methods, see M. P. Seah, Quantification of AES and XPS, in *Practical Surface Analysis, Second Edition, Vol. 1—Auger and X-ray Photoelectron Spectroscopy*, ed. C. D. Briggs and M. P. Seah, Wiley and Sons, NY, 1990.
- M. Xu, D. Fujita, J. Gao and N. Hanagata, *ACS Nano*, 2010, **4**, 2937–2945.
- V. K. Lazarov, R. Plass, H. Poon, D. K. Saldin, M. Weinert, S. A. Chambers and M. Gajdardziska-Josifovska, *Phys. Rev. B: Condens. Matter Mater. Phys.*, 2005, **71**, 115434.
- P. Merel, M. Tabbal, M. Chaker, S. Moisa and J. Margot, *Appl. Surf. Sci.*, 1998, **136**, 105–110.
- D. Caceres, I. Colera, I. Vergara, R. Gonzalez and E. Roman, *Vacuum*, 2002, **67**, 577–581.
- G. Kresse and J. Hafner, *Phys. Rev. B: Condens. Matter Mater. Phys.*, 1993, **47**, 558–561.
- G. Kresse and J. Furthmüller, *Comput. Mater. Sci.*, 1996, **6**, 15–50.
- G. Kresse and J. Furthmüller, *Phys. Rev. B: Condens. Matter Mater. Phys.*, 1996, **54**, 11169–11186.
- J. P. Perdew, K. Burke and M. Ernzerhof, *Phys. Rev. Lett.*, 1996, **77**, 3865–3868.
- G. Kresse and D. Joubert, *Phys. Rev. B: Condens. Matter Mater. Phys.*, 1999, **59**, 1758–1775.
- S. Grimme, J. Antony, S. Ehrlich and H. Krieg, *J. Chem. Phys.*, 2010, **132**, 154104.
- K. V. Emtsey, F. Speck, T. Seyller and L. Ley, *Phys. Rev. B: Condens. Matter Mater. Phys.*, 2008, **77**, 155303.
- G. Ertl and J. Kuppers, *Low energy electrons and surface chemistry*, Verlag-Chemie, Weinheim, FRG, 1974, pp. 129–188.
- M. Kiguchi, S. Entani, K. Saiki, T. Goto and A. Koma, *Phys. Rev. B: Condens. Matter Mater. Phys.*, 2003, **68**, 115402.
- A. Politano and G. Chiarello, *Nanoscale*, 2014, **6**, 10927–10940.
- L. J. Clarke, *Surface crystallography; an introduction to low energy electron diffraction*, Wiley and Sons, Chichester, UK, 1985.
- K. Krishnamoorthy, M. Veerapandian, K. Yun and S.-J. Kim, *Carbon*, 2013, **53**, 38–49.
- X. Diez-Betriu, S. Alvarez-Garcia, C. Botas, P. Alvarez, J. Sanchez-Marcos, C. Prieto, R. Menedez and A. de Andres, *J. Mater. Chem. C*, 2013, **1**, 6905–6912.

- 33 J. A. Kelber, M. Zhou, S. Gaddam, F. Pasquale, L. Kong and P. A. Dowben, *ECS Trans.*, 2012, **45**, 49–61.
- 34 S. M. Hafiz, R. Ritikos, T. J. Whitcher, N. M. Razib, D. C. S. Bien, N. Chanlek, H. Nakajima, T. Saisopa, P. Songsiririthigul, N. M. Huang and S. A. Rahman, *Sens. Actuators, B*, 2014, **193**, 692–700.
- 35 R. Furue, E. P. Koveke, S. Sugimoto, Y. Shudo and S. Hayami, *Sens. Actuators, B*, 2017, **240**, 657–663.
- 36 K. Lian, Y. Ji, X. Li, M. Jin, D. Ding and Y. Luo, *J. Phys. Chem. C*, 2013, **117**, 6049–6054.
- 37 J. Kelber, J. Jones, B. Beauclair, O. Olanipekun, S. Lightbourne, M. Zhang, B. Pollok, J. Beatty, M. S. Driver, T. Cheng, Y. Liu and W. A. Goddard III, Direct growth of graphene on dielectric substrates: epitaxy at incommensurate and reactive surfaces, *Proceedings of the 13th Int. Conf. on Silicon and Integrated Circuit Technology (ICSICT)*, Hangzhou, China, August 3rd, 2017, DOI: 10.1109/ICSICT.2016.7998954.
- 38 R. Choudhary, P. Kumar, P. Manchanda, D. J. Sellmyer, P. A. Dowben, A. Kashyap and R. Skomski, *IEEE Magn. Lett.*, 2016, **7**, 3101604.